ORNL/SPR-2018/780
Rev. 0

Preliminary Characterization and Mechanical Performance of Additively Manufactured HT9

Nuclear Technology Research and Development

Prepared for
U.S. Department of Energy
Advanced Fuels Campaign
N. Sridharan and K.G. Field
National Laboratory
February 22nd, 2018
NTRD-M3NT-2018-OR020202071

SUMMARY

Laser-blown powder deposition of HT9 was performed to evaluate the feasibility of using advanced manufacturing to fabricate creep strength enhanced ferritic steels. The as-printed materials were tensile tested at room temperature, 330°C, and 550°C to provide a baseline value for the strength levels. The as-fabricated strengths are then compared with wrought materials in the published literature. The strength parameters for the as-fabricated HT9 was found to be significantly higher than that of wrought HT9 without sacrifice in ductility. Two different heat treatment cycles, deemed ACO3 and FCRD, involving two different austenitizing temperatures (ACO3: 1065˚C and FCRD: 1040˚C) and tempering temperatures (ACO3: 750˚C and FCRD: 760˚C) were then evaluated. The heat-treated samples were also tensile tested and were found to show strength and ductility parameters which closely mimicked that of the wrought HT9 literature data.

Detailed multi-scale characterization was performed at various length scales. The as-fabricated structure showed a refined martensitic structure with a significant fraction of δ-ferrite present. Closer examination using TEM showed a refined distribution of carbides (predominantly $M_{23}C_6$ and MX or M_2X), which would have precipitated during the deposition process. Upon heat treatment, it was seen that the precipitates were more homogenous and refined in the case of the specimens heat treated according to the ACO3 cycle although there was no significant difference in the strength or the hardness results. However, the specimens heat-treated per the FCRD cycle showed significantly smaller prior austenite grains, which could result in better Charpy toughness. However, the toughness was not evaluated and will be performed in the future. In addition, possible thermo-mechanical treatments (TMT) to refine the grain structure and improve the toughness without compromising the ductility will also be evaluated in the future.

CONTENTS

FIGURES

ACRONYMS

C	Carbon
CALPHAD	Computer Coupling of Phase Diagrams and Thermochemistry
Cr	Chromium
DMD	Directed Metal Deposition
dpa	Displacements per atom
EBR-II	Experimental Breeder Reactor II
EBSD	Electron Backscattered Diffraction
EDS	Energy Dispersive X-ray Spectroscopy
FFTF	Fast Flux Test Facility
FM	Ferritic-martensitic
HIC	Hydrogen Induced Cracking
Mo	Molybdenum
N	Nitrogen
Nb	Niobium
SEM	Scanning Electron Microscopy
STEM	Scanning Transmission Electron Microscopy
TEM	Transmission Electron Microscopy
V	Vanadium
W	Tungsten
Wt.%	Weight Percent

PRELIMINARY CHARACTERIZATION AND MECHANICAL PERFORMANCE OF ADDITIVELY MANUFACTURED HT9

1. INTRODUCTION

High chromium ferritic-martensitic (FM) steels are candidate materials for advanced nuclear power plant designs where they are considered for use as cladding, wrappers, and ducts [1, 2]. This is because of their excellent thermal properties and low swelling characteristics compared to their austenitic stainless steel counter parts [3]. The workhorse alloys among FM steels for nuclear applications are HT9 (12Cr-1MoVW, in wt.%) and P91 (9Cr-1MoV, in wt.%) [1]. While HT9 is considered to be a first-generation FM steel which has been supplanted by the more advanced P91 for use in the fossil industry, the steel is of significant interest to the nuclear power generation community primarily due to the extensive irradiation performance database from the Experimental Breeder Reactor-II (EBR-II) and the Fast Flux Test Facility (FFTF). This irradiated materials database shows excellent swelling and creep resistance relative to the other materials tested [4]. In one specific case, at the maximum swelling temperature of 400-420˚C less than 2% swelling was observed for HT9 and P91 irradiated to 200 dpa in the FFTF [5]. Different researchers have tested multiple heats of HT9 in the past for their yield strength, fracture toughness, impact toughness, and thermal creep strength.

The rich irradiated materials database on HT9 has prompted commercial startup companies such as TerraPower, LCC to revitalize the manufacturing of HT9 [6]. While HT9 has been fabricated by using thermal mechanical processing, the steps involve significant process control and inter-pass heat treatments to successfully fabricate large sections [7]. The sections then have to be welded often leading to the formation of intercritically-heated zones leading to the formation of Type IV zones, which may lead to deterioration in the creep rupture strength of the materials [8]. To circumvent this, several commercial nuclear companies are interested in evaluating additive manufacturing for the fabrication of these sections. Additive manufacturing is emerging as an attractive pathway to fabricate large sections of creep strength enhanced FM steels for nuclear applications. Here, we report on the preliminary results based on the fabrication of HT9 hex-duct like sections using Laser-blown powder additive manufacturing.

2. BACKGROUND

As mentioned previously, HT9 is a 12Cr-1MoVW alloy. The 12 wt.% Cr steels were developed to provide a substitute for low Cr steels and to permit manufacturing of components that could be used at temperatures at or above 600˚C in power generation plants [1-4, 9]. Mo and W additions serve to increase the strength of these steels. Design of these steels requires balancing of the ferrite formers and the austenite formers to avoid the formation of δ-ferrite. δ-ferrite formation in FM steels is known to be detrimental to the toughness, mechanical properties and radiation resistance of these steels. These steels also benefit from the intentional addition of N, which is also a powerful austenite stabilizer. The addition of W, V, Mo and C promotes the precipitation of carbides and carbonitrides leading to secondary strengthening [1, 2]. In the normalized condition, the microstructure essentially consists of martensite laths with a high dislocation density (10^{10}-10^{14} m^{-2}) [9, 10]. However, during tempering the dislocations recover and the laths become elongated sub-grains. Upon tempering the primary precipitate microstructure is the coarse (60-150 nm) $M_{23}C_6$ carbides and to a lesser extent MX precipitates (V- and Nb-rich) which are much finer (20-80nm) [9]. The $M_{23}C_6$ carbides stabilize the lath boundaries while the MX precipitates serves to pin mobile dislocations; both processes retard recovery. While these are equilibrium carbides, the precipitation sequence in these alloys is complex and is a strong function of the composition of the steel. For instance, during tempering of HT9 at 700˚C for 15 minutes, the first phases to form are M_7C_3 and $M_{23}C_6$. The M_7C_3 then transforms to $M_{23}C_6$ at the end of the tempering treatment

[9]. These precipitates are important not just from a creep resistance aspect but also from a radiation resistance stand point. The reason being that the precipitate matrix interfaces and defects serve as point defect annihilation sites thereby improving the void swelling characteristics of the alloy [11].

Additive manufacturing is a layer-wise building of a part by depositing metal powder using fusion methods [12] or solid state [13]. Here, we explore the Laser-blown powder direct energy deposition process for production of HT9 with suitable microstructures for nuclear power applications. The process essentially consists of a nozzle that deposits powder into a melt pool created by a coaxial laser beam. The head is capable of moving in the X, Y, and Z directions thus being able to deposit any geometry [14]. However this layer-wise deposition means that each layer undergoes multiple heat treatments during deposition of the next layer [15]. This phenomenon introduces additional complexities over traditional wrought processing as the prior austenite grain size, precipitate size distribution, and precipitate volume fraction is a strong function of the austenitizing treatment temperature, soaking time, tempering temperature and time. However, in the case of additive manufacturing it becomes extremely difficult to control the microstructure and obtain a homogenous microstructure due to the sharp thermal gradients and the thermal cycling the material undergoes [15, 16]. The continuous deposition of build layers results in the flow of heat to previously deposited layers resulting in a unique thermal cycle along the length of the build of any given component. The degree of variability in the thermal cycling is a strong function of the process parameters.

In FM steels that are additively manufactured, the important transformations include the Ac_1, Ac_3 and the solidus isotherms in the heat affected zones. The regions above the Ac_3 and below the solidus are completely re-austenized and the regions between Ac_1 and Ac_3 transforms to austenite partially. Regions heated below the Ac_1 are only tempered. However, parallels may be drawn to microstructure evolution during multi-pass welding. The effects of such thermal cycles during multi-pass welding of a modified 9 wt.% Cr FM steel have been well documented. Due to the synergistic aspects of multi-pass welding with additive manufacturing the literature on the phase transformations during welding of high Cr steels are reviewed.

The high Cr FM steels are often considered difficult to weld compared to their austenitic counterparts since these steels upon solidification air harden to form martensite and δ-ferrite [8]. The primary concern with martensite formation is the susceptibility of the microstructure to hydrogen induced cracking (HIC). The industry standard to prevent HIC is to maintain a preheat of at least 150˚C and an inter-pass temperature of at least 350˚C [8]. δ-ferrite formation could lead to significant reductions in toughness in the steels [8]. The δ-ferrite in these steels during welding could either occur during,

a) solidification where the δ-ferrite is the first phase to form. The δ-ferrite then transforms to austenite via a peritectic reaction. The austenite then transforms to martensite. However, the reaction in many cases could be incomplete where the δ-ferrite may not always transform to austenite due to the rapid cooling rates typical of the welding processes. Since the cooling rates in additive manufacturing are comparable/higher than those occurring during welding δ-ferrite formation during additive manufacturing is expected [17].

b) δ-ferrite also forms during reheating of the deposited weld metal. During the deposition of the n^{th} layer the $(n-1)^{th}$ layer is reheated as discussed previously. When heated to a temperature between the solidus temperature T_m and the $T_{\delta\gamma}$ ferrite the room temperature microstructure transforms to a microstructure containing δ-ferrite and austenite. On cooling the austenite transforms to martensite while the δ-ferrite is retained [17].

Weld solidification dynamics have been investigated in the past using CALPHAD techniques [18, 19]. For instance, during fabrication of P91 steels it has been reported that the primary phase to solidify is δ-ferrite and that towards the end of solidification the inter-dendritic regions get enriched in austenite stabilizing elements such as C and N [19]. Based on this it was hypothesized that the solidifying weld

metal should show a large range over which the transformation from austenite to martensite would occur leading to a possibility of retained austenite formation in the weld. The impact of this micro segregation on the transformation behavior has been studied and discussed using TRXRD experiments [8]. This mechanism of retained austenite formation can also occur during additive manufacturing of HT9. During the deposition of the next pass the previous pass may see various peak temperatures [20].

i) A coarse grain heat affected zone where the temperature is above the Ac_3 leading to the dissolution of the carbides resulting in complete austenite grain growth

ii) A fine grain heat affected zone where the peak temperature reaches just above the Ac_3

iii) An inter critical heat affected zone where the temperature is between the Ac_1 and Ac_3

iv) An over tempered zone where the peak temperature is below Ac_1

While attempting to fabricate 9-12 %Cr creep strength enhanced ferritic steels using additive manufacturing of these steels one needs to be cognizant of liquid→solid phase transformation and also solid→solid phase transformations occurring in these steels. This report details the preliminary attempts to fabricate HT9 builds using additive manufacturing for the first time taking these considerations into account.

3. EXPERIMENTAL PROCEDURE

HT9 powder feedstock with a size range of 40-120 μm diameter was-fabricated using gas atomization. The builds were fabricated using a DMD 103D blown powder additive manufacturing process. The laser used was a 1 kW diode laser with a wavelength of 910 nm and a beam diameter of 1.5 mm. A portion of the build was held in reserve while additional sections were then heat treated using the heat treatment cycles shown in Figure 1.

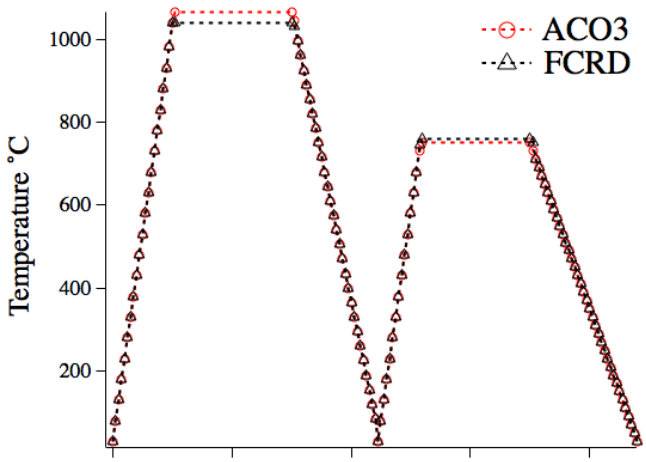

Figure 1: Heat treatment cycles for the AM-produced HT9. The samples were austenized at 1040˚C (FCRD) and 1065˚C (ACO3) for 30 minutes followed by air cooling and tempering at 760˚C (FCRD) and 750˚C (ACO3) respectively.

Following fabrication, SS-J3 miniature tensile specimens were machined out using electrode discharge machining. Tensile tests were conducted using shoulder loading at a strain rate of 10^{-3} s^{-1} in ambient air conditions. Tests were performed at room temperature, 330°C, and 550°C. Engineering stress-strain curves were constructed from the load-displacement curves. The fractured room temperature specimens were then mounted and polished using standard metallographic procedures and etched using Villelas reagent to reveal the prior austenite grain structure and carbide dispersions. Optical microscopy and

hardness testing were performed using an Olympus microscope and a Buehler hardness testing system using a load of 300 g with a dwell time of 10s.

Microstructural characterization was completed using scanning electron microscopy (SEM) on a JEOL 6500F field emission gun (FEG) SEM. SEM imaging was completed using an accelerating voltage of 20kV and a probe current of 4 nA. Electron backscatter diffraction (EBSD) was performed to characterize the martensite lath structure using identical imaging conditions. Specimens for transmission electron microscopy (TEM) were prepared from the polished specimens using standard focused ion beam (FIB) preparation on a Hitachi NB-5000 Focused Ion Beam FIB/SEM. TEM was performed using a FEI (now Thermo Fisher Scientific) Talos F200X scanning transmission electron microscope (S/TEM) operating at 200 kV.

4. RESULTS AND DISCUSSIONS

4.1 Mechanical Performance

The results from the tensile tests on sub-sized SS-J3 specimens are summarized in Figure 2 and compared directly towards historical wrought data extracted from Xu and Hackett [6]. The as-built AM HT9 showed significant increases in the yield strength and the ultimate tensile strength compared to the historical wrought data across all temperatures tested. In additional, a clear anisotropy exists, with the strength of the material being weaker in the Z-direction (direction of build) compared to that of the X/Y-direction. Given the increased strengths in the as-built specimens, the total elongation values were on par with that of the wrought HT9 but the X/Y-direction, which exhibited the highest strength, was reduced compared to the historical values. Interestingly, the X/Y-direction shows a decrease in total elongation with increased test temperature suggesting different deformation mechanics compared to that of the wrought material. This could be due to the vastly different precipitate structure in the as-built HT9 compared to more traditionally normalized and tempered HT9.

The AM fabricated HT9 specimens that underwent either the ACO3 or FCRD heat treatment showed values similar to those of the wrought HT9 data for both the strength parameters and the total elongation. Furthermore, the strong anisotropy in the mechanical properties of the as-built HT9 material is significantly reduced for both heat treatment conditions, especially when tensile tests are performed at 330°C or lower. The observed lack of anisotropy after heat treatment suggests that a “memory effect” does not exist for the AM components after elevated temperature heat treatments. The FCRD heat treated specimens in both orientations showed improved ductility compared to wrought HT9 indicating that the mechanical properties of the AM produced HT9 components could be controlled by closely determining a prescribed heat treatment schedule as part of a post processing step.

Hardness measurements were also performed to investigate the influence of processing and heat treatments on the hardness. The as-built microhardness was measured as 365 ± 22 VHN while the heat treatments of ACO3 and FCRD showed values of 256 ± 5 VHN and 239 ± 6 VHN, respectively. The hardness measurements show that the as-fabricated samples have significant scatter (~50 VHN) while the samples after heat treatment do not show any major fluctuations. The scatter in the as-fabricated hardness could be a result of the precipitation of δ-ferrite which could lead to localized reductions in the hardness values. The ACO3 treatments show a slight increase in the hardness compared to the FCRD. This could be due to the fact that the carbide distribution in the ACO3, as discussed in later sections, is much finer contributing to increased secondary hardening.

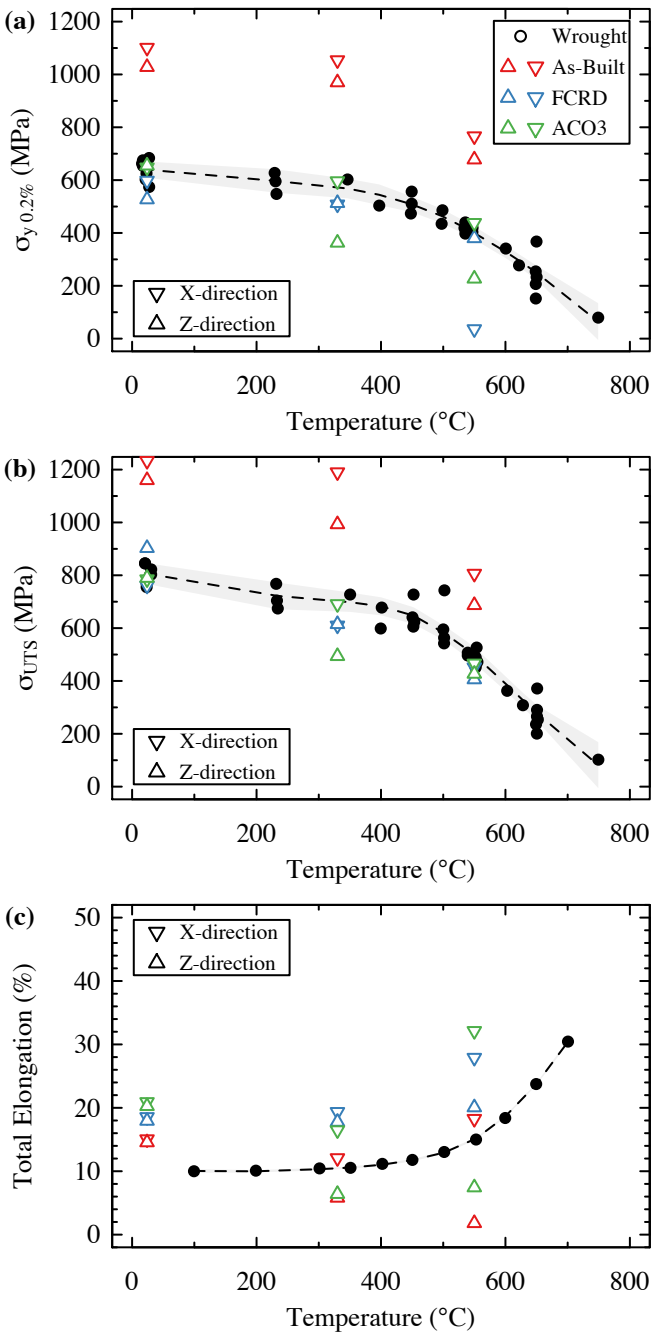

Figure 2: Comparison of historical wrought HT-9 [6] to additive manufactured HT-9 in the as-built condition, FCRD heat treatment, and ACO3 heat treatment tensile properties including (a) yield strength - $\boldsymbol{\sigma_{y\,0.2\%}}$, (b) ultimate tensile strength - $\boldsymbol{\sigma_{UTS}}$, and (c) total elongation.

4.2 Microstructure characterization

Most 9-12 wt.%Cr FM steels have a three-level hierarchical microstructure consisting of laths, blocks, and packets. The fundamental building block of these steels are the individual martensitic laths. These laths have a significant concentration of defects and precipitates which can aid in the creep strength and radiation tolerance. Laths with identical orientation are grouped into blocks. The blocks that form a single $\{111\}_\gamma$ are further grouped into packets. Ideally one block can have 6 different blocks if the Kurdjumov-

Sachs (K-S) orientation relationship is satisfied [21]. However, often variant selection occurs and therefore all 6 blocks do not form and it has been reported that in certain highly alloyed steels the packets have a bi-variant structure [22]. The characterization campaign was performed to qualitatively understand the effect of processing on,

1. Carbide sizes and volume fraction
2. Martensite lath sizes
3. Martensite block size
4. Prior austenite grain size in the sample.

Multiscale characterization ranging from optical microscopy, SEM-EBSD, and S/TEM were employed to characterize these features to understand the role of processing on microstructure.

4.2.1 General observations of as-fabricated samples

The microstructure of the as-fabricated samples is shown in Figure 3. Figure 3(a)&(c) shows the optical microstructure of the as-fabricated sample. The as-fabricated structure consists of a significant fraction of δ-ferrite in the build. Note, the δ-ferrite occurs at regular intervals. This suggests that the formation of δ-ferrite occurs primarily due to reheating layers during the build. On closer examination, the δ-ferrite is found to be predominantly polygonal δ-ferrite, which is known to form during welding of 9-12 wt.% Cr steels with a very high Cr equivalent [8].

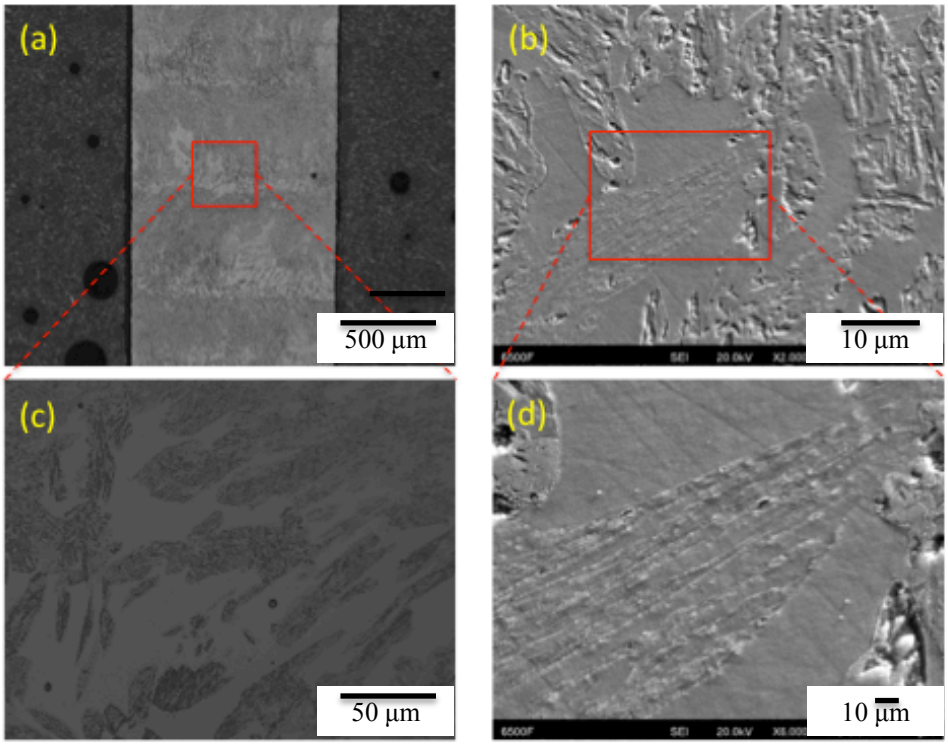

Figure 3: Optical and SEM micrographs of the as-fabricated samples. (a) and (c) Optical micrographs showing the extensive amount of delta ferrite and martensitic structure. (b) and (d) SEM micrographs showing the ultra-fine precipitation of the carbides in the martensite laths.

The optical micrographs also show that the prior austenite grains are significantly refined. This could be attributed to the multiple inter-critical heat treatments that these zones underwent leading to the breakdown of the columnar structure as shown by Evans [23]. SEM observations also confirms the

presence of δ-ferrite and EDS was not able to detect any differences in the Cr segregation behavior. The results from the SEM analysis are presented in Figure 3(b)&(d). Figure 3(b) clearly shows that the prior austenite grains have an ultra-fine grain size with the martensite mostly being lath martensite with minor constituents of plate martensite. The SEM micrographs presented in Figure 3(d) also shows evidence of a refined distribution of carbides within the martensite laths and no precipitates occurring within the δ-ferrite. While we were not able to detect any precipitates within the δ-ferrite grains, previous studies have shown the precipitation of needle like MX within the grains, which nucleate at higher temperatures during solidification or re-heating in multi-pass welds [24]. TEM was performed to identify the precipitates in the builds and the results will be discussed in a later part of this work.

4.2.2 General observations of ACO3 heat treated samples

The ACO3 heat treatment involved austenitizing the as-built sample to a temperature of 1065˚C and soaking it for 30 minutes followed by air cooling and tempering at 750˚C for 1 hour followed by air cooling, Figure 1. The microstructural observations are summarized in Figure 4(a)-(d). Figure 4(a)&(b) show the optical micrographs of the sample after heat treatment. The optical micrograph primarily shows that the δ-ferrite has been effectively eliminated during re-austenization and that significant austenite grain growth has occurred during the austenization (Fig. 4c). The result is a coarse prior austenite grain structure compared to the as-fabricated microstructure. The tempering treatment also shows a uniform distribution of carbides along the prior austenite grain boundaries and inside the martensite laths (Fig. 4d and 4e).

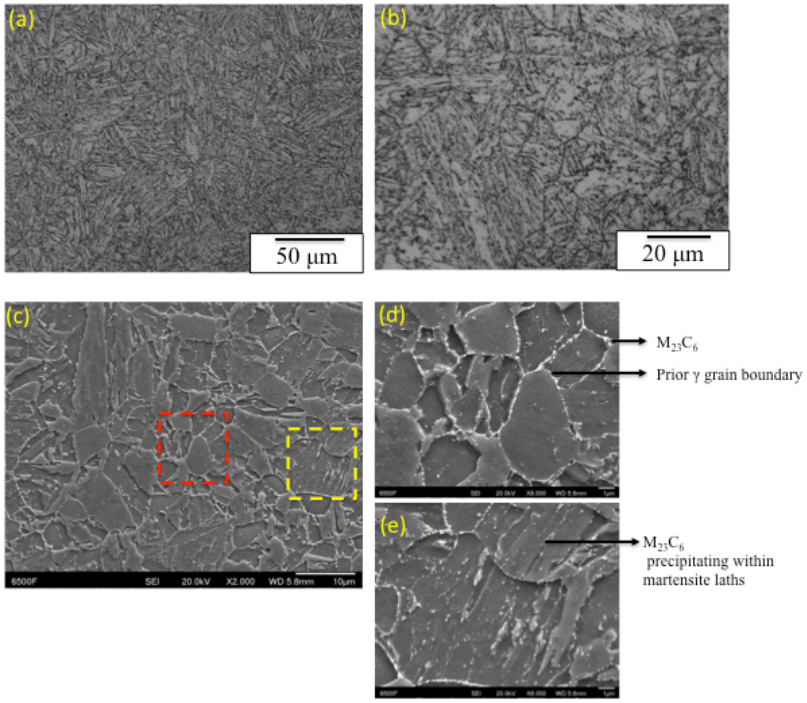

Figure 4: Microstructure of HT9 specimens after ACO3 treatment (a)-(b) Optical micrograph showing the tempered martensite structure with a significant amount of carbide precipitates (c) SEM micrograph showing the presence of $M_{23}C_6$ precipitates decorating the prior austenite grain boundary (d) Higher magnification the region marked using a red box in figure (c) (e) Higher magnification (marked with a yellow box) showing inter and intra lath precipitation of carbides.

4.2.3 General observations of FCRD heat treated samples

The FCRD heat treatment involved austenitizing the as-fabricated sample to a temperature of 1040˚C and soaking it for 30 minutes followed by air cooling and tempering at 760˚C for 1 hour followed by air cooling, Figure 1. The microstructural observations are summarized in Figure 5(a)-(d). Figure 5(a)&(b) show the optical micrographs of the sample after heat treatment. The optical micrographs primarily show that the δ-ferrite has been effectively eliminated during re-austenization similar to what had been observed during the ACO3 treatments. Since the austenization temperature was lower than the ACO3 treatment, the austenite grain growth is also limited compared to that of the ACO3 heat treatment. The prior austenite grain size is also significantly finer. This could be attributed to the fact that some fraction of the V-rich MX precipitates did not dissolve during the heat treatments therefore pinning the boundaries. V-rich MX precipitates have been reported to be present during the final cool down in multi-pass welds and therefore would be expected to be present in the as-fabricated microstructure. The SEM micrographs presented in Figure 5(c)&(d) also show a significant coarsening of the carbides that are present within the martensite laths. This could be due to the fact that these carbides did not dissolve during austenization and during tempering simply coarsened these carbides. Also, note that the tempering treatment also shows that the carbides have coarsened significantly during tempering and are not present only on prior austenite grain boundaries but also a significant fraction is present in the martensite lath boundaries as well.

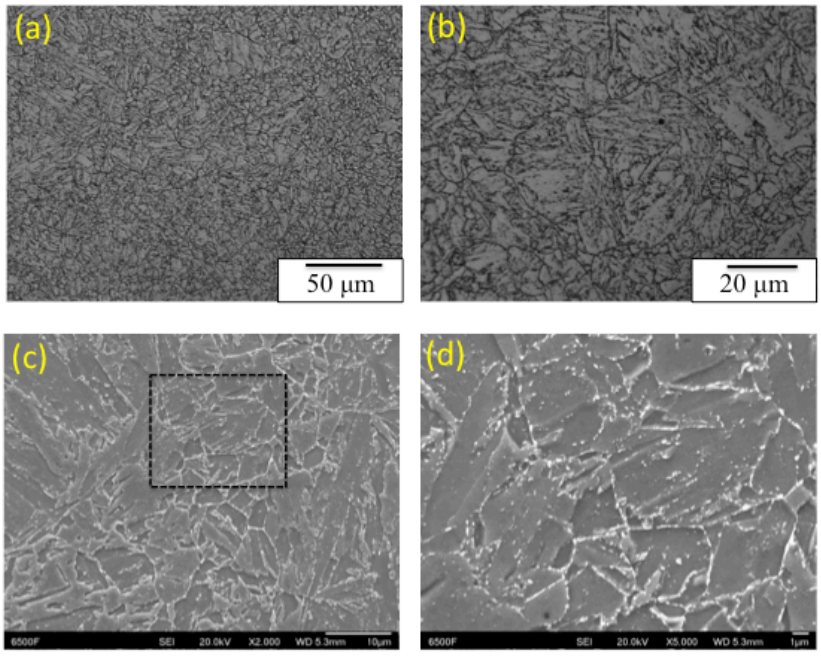

Figure 5: Microstructure of HT9 specimens after FCRD treatment (a)-(b) Optical micrograph showing the tempered martensite structure with a significant amount of carbide precipitates. Note the finer PAGS and the coarser carbide distribution. (c) SEM micrograph showing the presence of $M_{23}C_6$ precipitates decorating the prior austenite grain boundary. However, significant fraction of precipitates is observed which pin the martensite sub grains (d) Higher magnification of the region marked using a black box in figure (c) showing the intra lath precipitation showing that the carbides in the as-fabricated specimens have not dissolved during the austenization treatment.

4.2.4 Measurements of grains, packets and block sizes

EBSD was performed to measure the prior austenite grain sizes, the lath sizes, and block sizes of martensite after heat treatments. Based on the crystallography of martensitic transformation it has been shown previously that each block will have a misorientation of 10.53˚ along the ⟨110⟩ and the prior austenite grains should have a misorientation of 20-45˚ and martensite packets should have a misorientation between 47-60˚ and therefore can be calculated using these well-established relations from an EBSD micrograph [21]. These measurements are necessary to be performed in these steels since in addition to precipitation strengthening these steels are also strengthened by sub-grain boundary strengthening and to retain strength it is essential that the laths and packets retain a fine grain structure. In addition, it has been demonstrated that the critical event for cleavage fracture initiation in HT9 is the propagation of a micro-cracking out of prior austenite boundary carbides. High angle boundaries serve to arrest/deflect cracks thereby leading to an increase in toughness and therefore a finer packet size and prior austenite grain size is effective in improving toughness as well. Therefore, a determination of the lath sizes, block sizes packet sizes and PAG size as a function of processing conditions is warranted.

The electron backscatter diffraction micrographs are presented in Figure 6(a)-(c). Figure 6(a) corresponds to a region in the as-fabricated sample, Figure 6(b) represents the samples heat treated using the ACO3 treatment, and Figure 6(c) represents the samples heat treated using the FCRD treatment. One prior austenite grain has been marked and 4 martensite blocks have been identified and marked as shown in Figure 6(b) and (c). Note that the number of blocks in each prior austenite vary between 3 and 4. This is indicative of a variant selection, which normally occurs in steels. The prior austenite grains were reconstructed using the procedure described earlier and are shown in Figure 7(a)-(c). Note Figure 7 provides a different field-of-view compared to Figure 6. The data clearly shows that differences in the grain structure from the as-fabricated and the post weld heat treated samples.

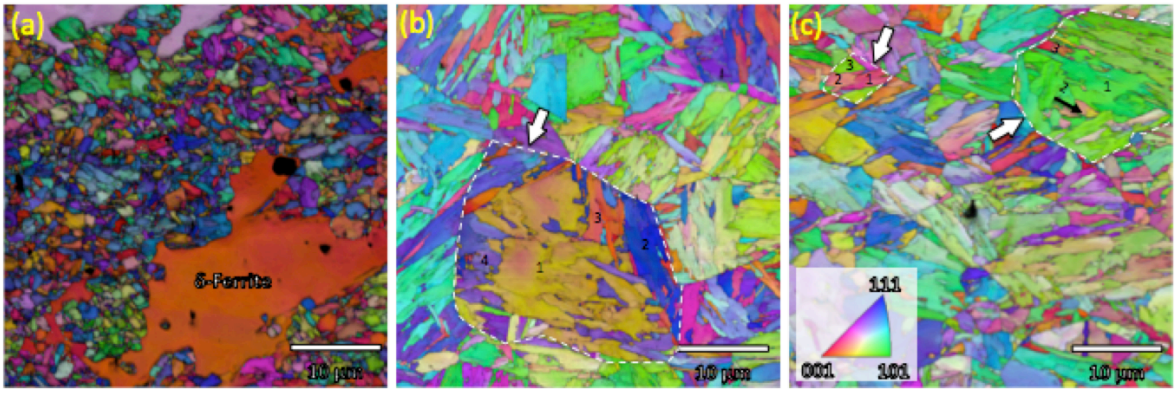

Figure 6: Electron back scatter diffraction micrographs for the (a) As-fabricated sample showing the presence of large polygonal δ-ferrite which is characteristic when the δ-ferrite phase is present in large volume fractions (b) ACO3 heat treated sample. Once prior austenite grain boundary has been marked (white dotted line and a white arrow) and 4 blocks have been identified and marked. (c) FCRD heat treated samples. Two prior austenite grains are marked (white dotted line with a white arrow) and the blocks are marked.

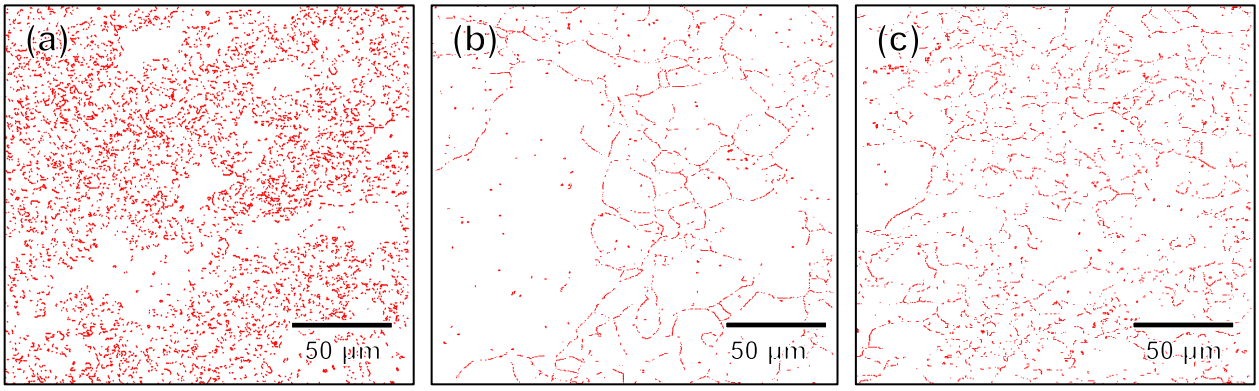

Figure 7: Prior austenite grain reconstructions for (a) as-fabricated (b) heat treated in the ACO3 cycle and (c) heat treated using the FCRD cycle.

4.2.5 Carbide identification and tempering response

Preliminary microstructure characterization was completed to measure the carbide sizes and the carbide area fraction as a function of heat treatments. Following this, a systematic S/TEM campaign to characterize the chemistry of the carbides and martensite lath size was initiated. The S/TEM results from the as-fabricated structure and the heat-treated specimens are presented in Figure 8(a)-(c). Note that the martensite laths are much finer in the as-fabricated sample and the line defects in the martensite laths coalesce to form sub grains leading to the coarsening of the lath structure. The laths are coarser for the FCRD treatments compared to the ACO3 treatments primarily due to the higher tempering temperatures of the FCRD treatment. The tempering treatments also resulted in the coarsening of the carbides which can be seen as the dark-contrast particles with polygonal shape in Figure 8. Note, the significant coarsening of the carbides in the FCRD treatment compared to the as-built and the ACO3 treatments.

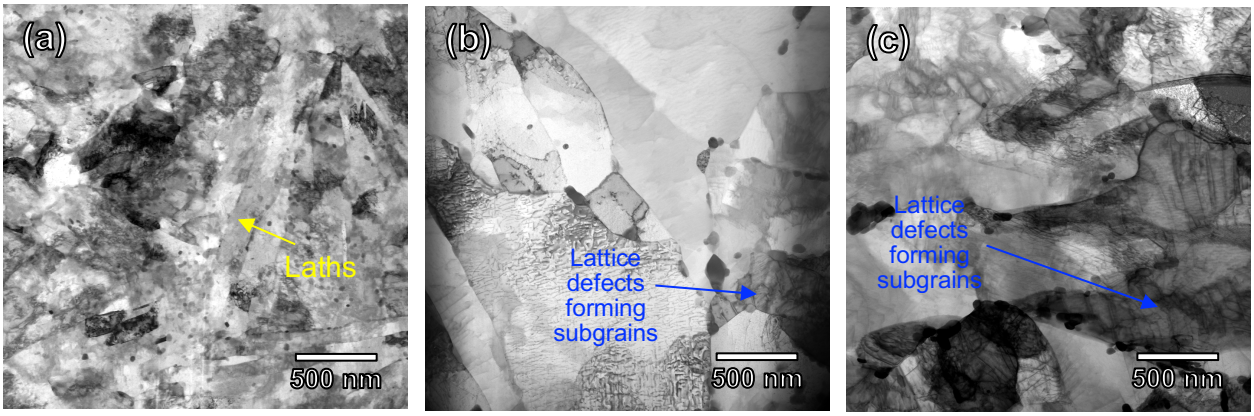

Figure 8: STEM BF micrographs of the (a) As-fabricated samples (b) After ACO3 treatments (c) After FCRD treatments showing the progressive coarsening of the lath substructure and the carbides

Diffraction patterns were taken from the matrix and the carbides with the matrix along the [111] zone axis. The diffraction patterns confirm that the coarse carbides identified in the figures are indeed $M_{23}C_6$. Figure 9 shows a micrograph with a carbide and the corresponding diffraction pattern where the carbide was indexed as $M_{23}C_6$.

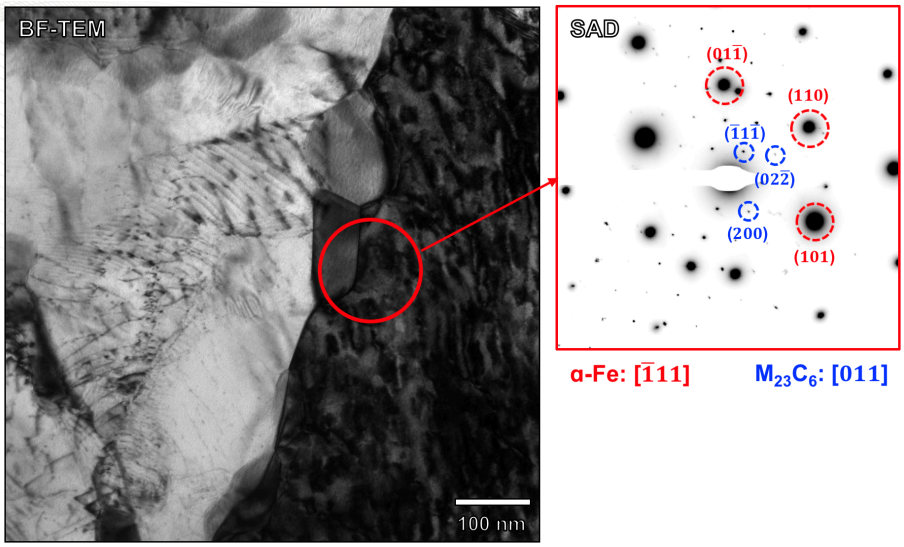

Figure 9: BF TEM micrograph and diffraction pattern indexing the large coarse carbides forming during tempering as $M_{23}C_6$.

5. SUMMARY AND CONCLUSIONS

Based on the preliminary results it is clear that defect-free creep strength enhanced ferritic steels can be effectively manufactured using Laser-blown powder additive manufacturing with acceptable mechanical properties. Based on the preliminary task that has been performed, it is clear that blown powder additive manufacturing is a viable processing technique to fabricate large structures such as clads, wrappers and ducts for the next generation advanced reactor concepts. Two different heat treatments have been evaluated and the microstructure evolution during post fabrication heat treatment has been evaluated. However, the fracture toughness behavior of these steels in the as-fabricated and post weld heat treated condition need to be evaluated. The influence of radiation on the mechanical properties and void swelling also needs to be evaluated.

6. REFERENCES

[1] R.L. Klueh, Elevated temperature ferritic and martensitic steels and their application to future nuclear reactors, International Materials Reviews 50(5) (2005) 287-310.

[2] R.L. Klueh, A.T. Nelson, Ferritic/martensitic steels for next-generation reactors, Journal of Nuclear Materials 371(1) (2007) 37-52.

[3] R.L. Klueh, D.R. Harris, High-Chromium Ferritic and Martensitic Steels for Nuclear Applications (ASTM, Conshohocken, 2001), Google Scholar.

[4] T.R. Allen, J.T. Busby, R.L. Klueh, S.A. Maloy, M.B. Toloczko, Cladding and duct materials for advanced nuclear recycle reactors, JOM Journal of the Minerals, Metals and Materials Society 60(1) (2008) 15-23.

[5] D.S. Gelles, Effects of irradiation on ferritic alloys and implications for fusion reactor applications, Journal of Nuclear Materials 149(2) (1987) 192-199.

[6] C. Xu, M. Hackett, TerraPower HT9 Mechanical and Thermal Creep Properties, Mechanical and Creep Behavior of Advanced Materials, Springer2017, pp. 95-102.

[7] S.A. Maloy, M. Toloczko, J. Cole, T.S. Byun, Core materials development for the fuel cycle R&D program, Journal of Nuclear Materials 415(3) (2011) 302-305.

[8] S.A. David, J.A. Siefert, Z. Feng, Welding and weldability of candidate ferritic alloys for future advanced ultrasupercritical fossil power plants, Science and Technology of Welding and Joining 18(8) (2013) 631-651.

[9] R.C. Thomson, H. Bhadeshia, Carbide precipitation in 12Cr1MoV power plant steel, Metallurgical Transactions A 23(4) (1992) 1171-1179.

[10] J.M. Vitek, R.L. Klueh, Precipitation reactions during the heat treatment of ferritic steels, Metallurgical and Materials Transactions A 14(6) (1983) 1047-1055.

[11] G.R. Odette, M.J. Alinger, B.D. Wirth, Recent developments in irradiation-resistant steels, Annu. Rev. Mater. Res. 38 (2008) 471-503.

[12] N. Sridharan, M.W. Noakes, A. Nycz, L.J. Love, R.R. Dehoff, S.S. Babu, On the toughness scatter in low alloy C-Mn steel samples fabricated using wire arc additive manufacturing, Materials Science and Engineering: A 713 (2018) 18-27.

[13] N. Sridharan, M. Gussev, R. Seibert, C. Parish, M. Norfolk, K. Terrani, S.S. Babu, Rationalization of anisotropic mechanical properties of Al-6061 fabricated using ultrasonic additive manufacturing, Acta Materialia 117 (2016) 228-237.

[14] R.R. Dehoff, N. Sridharan, R. Dinwiddie, A. Robson, B. Jordan, A. Chaudhary, P.S.S. Babu, Demonstration of thermal control, microstructure control, defect mitigation and process parameter database generation for Ti-6Al-4V Direct Digital Manufacturing-Understanding defect mitigation and process parameter database generation for direct digital manufacturing, Oak Ridge National Laboratory (ORNL), Oak Ridge, TN (United States). Manufacturing Demonstration Facility (MDF), 2015.

[15] K.T. Makiewicz, Development of simultaneous transformation kinetics microstructure model with application to laser metal deposited Ti-6Al-4V and alloy 718, The Ohio State University, 2013.

[16] Y. Tian, D. McAllister, H. Colijn, M. Mills, D. Farson, M. Nordin, S. Babu, Rationalization of microstructure heterogeneity in Inconel 718 builds made by the direct laser additive manufacturing process, Metallurgical and Materials Transactions A 45(10) (2014) 4470-4483.

[17] J.C. Lippold, Welding metallurgy and weldability, John Wiley & Sons2014.

[18] S. Babu, Thermodynamic and kinetic models for describing microstructure evolution during joining of metals and alloys, International Materials Reviews 54(6) (2009) 333-367.

[19] S.S. Babu, S.A. David, M.L. Santella, J.M. Vitek, E.D. Specht, J.W. Elmer, Modelling and characterization of nonequilibrium weld microstructure evolution, na2003.

[20] R.C. Reed, H. Bhadeshia, A simple model for multipass steel welds, Acta metallurgica et materialia 42(11) (1994) 3663-3678.

[21] H. Kitahara, R. Ueji, N. Tsuji, Y. Minamino, Crystallographic features of lath martensite in low-carbon steel, Acta Materialia 54(5) (2006) 1279-1288.

[22] C.C. Kinney, K.R. Pytlewski, A.G. Khachaturyan, J.W. Morris, The microstructure of lath martensite in quenched 9Ni steel, Acta Materialia 69 (2014) 372-385.

[23] G.M. Evans, The Effect of Heat Input on the Microstructure and Properties of C--Mn All-Weld-Metal Deposits, Welding Journal 61(4) (1982) 125.

[24] G.-J. Cai, H.-O. Andrén, L.-E. Svensson, Effect of cooling after welding on microstructure and mechanical properties of 12 Pct Cr steel weld metals, Metallurgical and Materials Transactions A 28(7) (1997) 1417-1428.